Kent Academic Repository

Dickers, Matthew D., Fantuzzi, Felipe, Mason, Nigel, Sushko, Gennady B., Korol, Andrei V. and Solov’yov, Andrey V. (2026) *Structural effects of boron doping in diamond crystals for gamma-ray light-source applications: Insights from molecular dynamics simulations.* Diamond and Related Materials . ISSN 0925-9635.

Diamond & Related Materials 166 (2026) 113714

Contents lists available at ScienceDirect

Diamond & Related Materials

journal homepage: www.elsevier.com/locate/diamond

Structural effects of boron doping in diamond crystals for gamma-ray light-source applications: Insights from molecular dynamics simulations

Matthew D. Dickers [a],*, Felipe Fantuzzi [b], Nigel J. Mason [a], Gennady B. Sushko [c], Andrei V. Korol [c], Andrey V. Solov'yov [c]

[a] Physics and Astronomy, School of Engineering, Mathematics and Physics, University of Kent, Park Wood Rd, Canterbury CT2 7NH, UK
[b] Chemistry and Forensic Science, School of Natural Sciences, University of Kent, Park Wood Rd, Canterbury CT2 7NH, UK
[c] MBN Research Center, Altenhöferallee 3, 60438 Frankfurt am Main, Germany

ARTICLE INFO

Keywords:
Boron-doped diamond
Doped crystals
Inter-planar distance
Molecular dynamics

ABSTRACT

Boron-doped diamond crystals (BDD, $C_{1-x}B_x$) exhibit exceptional mechanical strength, electronic tunability, and resistance to radiation damage. This makes them promising materials for use in gamma-ray crystal-based light sources. To better understand and quantify the structural distortions introduced by doping, which are critical for maintaining channelling efficiency, we perform atomistic-level molecular dynamics simulations on periodic $C_{1-x}B_x$ systems of various sizes. These simulations allow the influence of boron concentration on the lattice constant and the (1 1 0) and (1 0 0) inter-planar distances to be evaluated over the concentration range from pure diamond (0%) to 5% boron at room temperature (300 K). Linear relationships between both lattice constant and inter-planar distance with increasing dopant concentration are observed, with a deviation from Vegard's Law. This deviation is larger than that reported by other theoretical and computational studies; however, this may be attributed to an enhanced crystal quality over these studies, a vital aspect when considering gamma-ray crystal light source design. The methodology presented here incorporates several refinements to closely reflect the conditions of microwave plasma chemical vapour deposition (MPCVD) crystal growth. These results enable reliable atomistic modelling of doped diamond crystals and support their use in the design and fabrication of periodically bent structures for next-generation gamma-ray light source technologies.

1. Introduction

Boron-doped diamond (BDD) has emerged as a versatile material with applications spanning electronics, sensing, and radiation technologies, owing to its exceptional mechanical hardness, thermal conductivity, and chemical stability. Incorporation of boron atoms into the diamond lattice introduces p-type semiconducting behaviour while preserving the intrinsic robustness of the host structure. This combination of structural and electronic properties makes BDD a valuable basis for both fundamental research and applied technologies, including electrochemical devices [1,2], quantum applications [3,4], and photodetectors [5,6]. Notably, the material has attracted recent interest in the development of crystal-based light sources (CLSs) operating in the gamma-ray regime, where its structural integrity and resistance to radiation damage are key for the controlled manipulation of particle beams [7–12].

Gamma-ray CLSs offer a novel method for generating high-brilliance, sub-angstrom wavelength electromagnetic radiation [7,10,11,13]. Such devices operate by directing beams of ultra-relativistic charged particles through the crystalline planes of oriented crystals where they undergo a process known as *channelling* [14]. The operation of these devices is based upon the emission of *channelling radiation*, which is emitted as charged particles oscillate within the potential wells formed by the crystalline planes [15]. The focus of this work concerns the structural properties of BDD crystals, which may be used to manufacture gamma-ray CLSs. A discussion of the theoretical foundations and physical mechanisms governing these processes is not provided here; these may be found in Refs. [7,10,11,13,16], which provide extensive overviews on this topic.

The properties of the emitted radiation are heavily dependent on the crystal's internal structure, with different internal geometries leading to the emission of different types of radiation. One particularly advantageous geometry is the periodically bent crystal, in which the crystalline planes are bent to follow a sinusoidal profile. The movement of charged particles along this periodic path results in the emission of *undulator*

---

* Corresponding author.
E-mail address: M.D.Dickers@kent.ac.uk (M.D. Dickers).

https://doi.org/10.1016/j.diamond.2026.113714
Received 16 September 2025; Received in revised form 4 May 2026; Accepted 4 May 2026

radiation [17], in addition to channelling radiation. This mechanism is closely analogous to that employed in modern free-electron lasers. This crystal geometry provides a high degree of tunability; by varying the bending amplitude and period, one can precisely control the spectral and angular properties of the emitted radiation.

Although numerous methods for the fabrication of bent crystals exist [17–32], the present study focuses on the approach of introducing spatially modulated dopant atoms into the crystal structure [33–35]. The incorporation of atoms with different covalent radii from those of the host lattice atoms leads to a local lattice mismatch. This mismatch induces an internal strain and leads to a change in the local geometry, displacing neighbouring atoms from their ideal crystallographic positions. Such impurity-induced distortions have been described in detail for doped $Si_{1-x}Ge_x$ crystals by Ref. [33], and the same physical principles apply to BDD systems. As the dopant concentration increases, the cumulative effect of these local distortions leads to a measurable change in the inter-planar distances. In the context of channelling in periodically bent crystals, where the (1 1 0) crystallographic planes are of most interest, a spatially varying dopant concentration along the axial length of the crystal (usually along the [1 0 0] direction) produces a periodic variation in the (1 1 0) inter-planar distances, and thus a bent channel through which charged particles may propagate. These dopant-induced lattice distortions directly influence the trajectories of channelled particles, and thus the production of undulator radiation. For an in-depth description of this mechanism, we direct the reader to Refs. [33,34,36]; this bending mechanism is illustrated in Figure 4 in Ref. [36]. In the case of BDD, boron atoms substitute directly for carbon atoms in the lattice; acting as substitutional point defects, they induce local strain due to their larger covalent radius ($0.88\,\text{Å}$ vs $0.77\,\text{Å}$ for carbon [37]), resulting in a net expansion of inter-planar distances.

BDD crystals may be fabricated using microwave plasma chemical vapour deposition (MPCVD) [8,38,39], in which a gas mixture of carbon-containing precursor molecules, such as methane (CH_4), is exposed to a microwave-induced plasma. The plasma decomposes the precursor molecule, allowing atomic carbon to deposit onto a substrate, typically high pressure high temperature (HPHT) synthetic type Ib diamond, chosen for its common availability and low cost. Depending on the substrate and growth conditions, this process produces either thin polycrystalline or homoepitaxial diamond films. For doped crystals, a controlled concentration of dopant precursor molecules is introduced during growth. In the case of boron doping, diborane gas (B_2H_6) is commonly used, with boron atoms incorporating substitutionally into the diamond lattice. To fabricate the periodically bent crystals used in gamma-ray CLS applications, the concentration of boron precursors in the gas mixture and the gas flow rate are periodically varied during the growth process to produce a spatially graded boron concentration along the length of the crystal. To provide a consistent designation of the boron content, the doped crystal is denoted as $C_{1-x}B_x$, where x represents the fractional concentration of boron atoms: $x = 0$ corresponds to undoped diamond, and $x = 1$ to a hypothetical lattice composed entirely of boron atoms. This notation will be used throughout this work, interchangeably with BDD.

The development of effective gamma-ray CLSs requires high-quality crystals with minimal structural defects. Low-quality crystals, characterised by point defects and dislocations [40], disrupt the periodic potential experienced by channelled particles and lead to dechannelling [14]: the premature exit of particles from the channelled trajectory. In this context, the quality of a CLS crystal can be quantified by the dechannelling length [14], the average distance a channelled particle travels before being dechannelled. Crystals of higher quality have fewer defects, and thus longer dechannelling lengths, leading to greater radiation intensity and improved CLS performance. Among the factors affecting crystal quality, dopant concentration plays a critical role: excessive doping introduces lattice strain and increases the likelihood of defect formation, which can degrade or eliminate channelling paths entirely. Careful control of dopant levels is therefore essential in crystal fabrication. In addition, the quality of the substrate significantly influences the quality of the grown crystal. Studies have demonstrated that type IIa HPHT diamond substrates yield higher-quality crystals compared to their type Ib counterparts [41]. Structural defects commonly present in type Ib substrates can propagate into the growing crystal, thereby reducing its crystalline quality. Consequently, the use of high-quality substrates is essential to achieve high-quality crystal growth.

A key advantage of $C_{1-x}B_x$ crystals is their demonstrated resistance to defect formation even at relatively high boron concentrations ($\sim 10^{21}$ atom cm^{-3}) [9,39]. Moreover, the strong C–C bonding in diamond provides exceptional lattice stability under high-energy particle irradiation [16,42,43], offering potentially longer operational lifetimes in CLSs compared to other systems such as $Si_{1-x}Ge_x$. These properties make $C_{1-x}B_x$ an especially promising material for the next generation of gamma-ray light sources.

Herein, we present a follow-up to our recent study [44] on the atomistic-level effects of germanium concentration on the structure of $Si_{1-x}Ge_x$ crystals. The present work investigates the influence of boron doping on the crystalline structure of diamond, incorporating several key improvements to the previous methodology of Ref. [44]. Specifically, the impact of boron atoms is examined across three distinct regions of the $C_{1-x}B_x$ crystal: near the substrate, within the bulk, and close to the free surface. The effects of different dopant concentration and crystal sizes on both the lattice constant and inter-planar distances are evaluated in each region. This analysis focuses on the (1 1 0) and (1 0 0) crystalline planes, which are particularly relevant to the doping strategies employed in the fabrication of CLS crystals. Across each simulation the dopant concentration is kept fixed, and crystals with spatially graded dopant concentrations that are typically used to fabricate periodically bent crystals are not modelled. This work instead focuses on the direct lattice response to dopant incorporation and does not model the MPCVD growth process. These results may be used to inform models for the design of periodically bent crystals for gamma-ray CLS applications.

Molecular dynamics (MD) simulations are performed using the MBN Explorer [45] and MBN Studio [46] software packages, enabling a detailed investigation of dopant-induced structural changes. These results are directly relevant to the design and practical realisation of gamma-ray CLSs, as reliable fabrication of periodically bent crystals requires a detailed understanding of manufacturing tolerances, especially concerning the maximum dopant concentration that can be introduced without compromising crystal quality.

The structure of this work is as follows. In Section 2.1, the computational methodology for generating and modelling $C_{1-x}B_x$ crystals is introduced, along with the range of crystal sizes and dopant concentrations considered. A geometric correction is presented in Section 2.2, that may be applied to the results to enable direct comparison with experimental and theoretical studies. Section 3.1 provides an overview of the structural metrics considered in this work, namely the lattice constant and inter-planar distances, with the corresponding simulation results reported in Sections 3.2 and 3.3, respectively. Finally, in Section 4, the implications of these results for the design and practical realisation of gamma-ray CLSs are discussed, along with prospects for methodological improvements and future research directions.

2. Methodology

2.1. Crystal structures and classification

This section outlines the computational methodology used to generate defect-free doped $C_{1-x}B_x$ crystals, and their subsequent atomistic-level analysis. All simulations were carried out using the MBN Explorer software package [45], designed for advanced multiscale modelling of complex molecular structures and dynamics. MBN Studio [46], a multitask toolkit and dedicated graphical user interface for MBN Explorer,

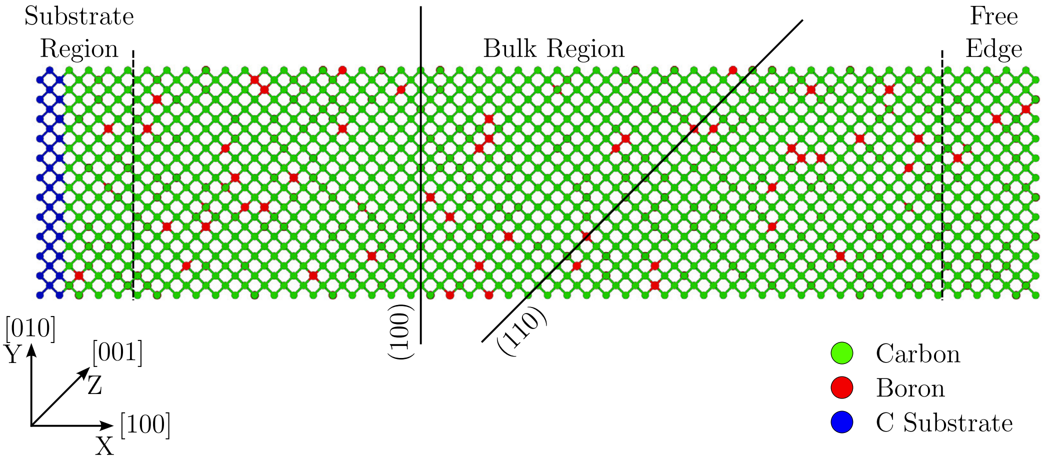

Fig. 1. Representative diagram of the crystal configuration used in the simulations. Carbon atoms are shown in green, boron atoms in red, and substrate carbon atoms in blue. The orientations of the (1 1 0) and (1 0 0) crystallographic planes are indicated by solid black lines, while the boundaries between the three analysis regions are marked by black dashed lines. Further details on these regions are provided in the text.

was utilised to construct the systems, prepare input files, and analyse simulation outputs. The methods used in this work are based on that presented in our previous study [44], with a number of notable improvements. Unlike the prior study, the present simulations are conducted under periodic boundary conditions at a fixed temperature of 300 K, corresponding to the canonical (NVT) ensemble. A range of crystal sizes with varying dimensions, denoted by L_X, L_Y, and L_Z, are considered. The specific crystal sizes and the rationale for their selection are outlined later in this section. To avoid confusion between spatial coordinates and dopant concentration, the coordinate directions are denoted as X, Y, and Z, while x is reserved for the dopant concentration. The structural configuration of the generated crystal is illustrated in Fig. 1: the system is periodic in the Y and Z directions, which serve as the lateral (transverse) directions, while the X direction is axial. A three-atom-thick carbon substrate is fixed at the base along the negative X-axis, constraining motion in that direction, while the positive X-axis is exposed to vacuum, allowing free expansion. This configuration enables subdivision of the crystal into three analysis regions, as shown in Fig. 1, which are described in detail later in this section.

BDD crystals were generated by first defining a single diamond unit cell in the MBN Explorer input file, which was then replicated along each axis to produce a crystal of a given dimension. In all simulations, Y and Z simulation box directions were fixed to match the corresponding crystal size. To ensure correct periodicity, the entire structure was offset by half the standard C–C bond length (0.77 Å) from the simulation-box edges. Because periodicity was required only along Y and Z, and MBN Explorer permits a single boundary condition per simulation, the box length along X was extended by 15 Å beyond the initial crystal length to allow free axial expansion and prevent interactions with periodic images. Although larger than the expected expansion, this buffer avoided artifacts and had a negligible impact on simulation time.

A pre-determined fraction of carbon atoms was then randomly selected and substituted with boron atoms, corresponding to target boron concentrations between $x = 0.00$ (0%) and $x = 0.05$ (5%, 8.82×10^{21} cm^{-3}) in increments of 0.01. In BDD crystals, dopant concentrations are usually small, in the region of $\lesssim 1\%$ [8,9] due to the limited solubility of boron in diamond (typically ∼1%–2%) [47]. Higher concentrations were included here to (i) reflect ranges considered in previous studies and (ii) evaluate structural effects at levels that may become achievable with future technologies. Because carbon atoms were selected at random for substitution by boron, the precise target concentration cannot be guaranteed. Calculations of the 'true' dopant concentrations show minimal deviation from the target values.

Table 1
Table of multi-component Tersoff potential [48,49] parameters for C-B. Parameters for C from Ref. [49] and parameters for B from Ref. [50]. Note that the parameters β, n, c, d, h, χ_{i-j}, and ω_{i-j} are dimensionless.

Elements	C [49]	B [50]
A (eV)	1.3936×10^3	2.7702×10^2
B (eV)	3.467×10^2	1.8349×10^2
λ (Å^{-1})	3.4879	1.9922
μ (Å^{-1})	2.2119	1.5856
β	1.5724×10^{-7}	1.6000×10^{-6}
n	0.72751	3.9929
c	3.8049×10^4	5.2629×10^{-1}
d	4.384	1.5870×10^{-3}
h	−0.57058	0.5000
R_{min} (Å)	1.8	1.8
R_{max} (Å)	2.1	2.1
Interactions $(i-j)$	C-B [50]	
χ_{i-j}	1.0025	
ω_{i-j}	1.0000	

A full breakdown for each target concentration and crystal size is provided in Tables S1–S5 of the Supplementary Information (SI), as well as a dedicated statistical. This random substitution method also assumes that boron atoms only occupy substitutional sites, and does not explicitly account for boron located at interstitial positions. As such, the resulting crystals correspond to the idealised case of fully substitutional BDD.

The substrate was generated to match each crystal's L_Y and L_Z dimensions, but truncated along L_X to a thickness of three atoms to minimise system size. In MPCVD growth, an HPHT synthetic type Ib diamond substrate is typically employed as the growth surface. In this work, the HPHT substrate is not explicitly modelled; instead, its structural support is mimicked by fixing all substrate atoms. Thermal vibrations were neglected during substrate generation, and the atoms were held fixed throughout the simulation, preventing expansion along the negative X direction. The substrate was positioned to the left of each crystal, with the interface aligned to preserve the diamond lattice. Atomic interactions were modelled using the multi-component Tersoff potential [48,49], with the specific parameters and interacting atoms summarised in Table 1.

A range of crystal sizes, varying in L_X, L_Y, and L_Z, was considered in this work to optimise and simplify the simulations while minimising the total number of atoms for computational efficiency. Lateral dimensions were analysed to elucidate their effect on the results, thereby

Table 2

Summary of all crystal configurations used in this study. Each structure is identified by a label and defined by its X, Y, and Z dimensions in Å, the total number of atoms in the crystal N_{crys}, the total number of atoms in the substrate N_{sub}, and the corresponding figure where the structure is shown. Figures denoted 'S' are located in the SI. In cases where two figure references are given the configuration appears in both.

Label	$L_X \times L_Y \times L_Z$ (Å)	N_{cry}	N_{sub}	Figure Ref.
C1	21.402 × 21.402 × 21.402	1800	216	Fig. 2/S1
C2	24.969 × 24.969 × 24.969	2842	294	Figure S1
C3	28.536 × 28.536 × 28.536	4224	384	Figure S1
E1A	89.175 × 21.402 × 21.402	7272	216	Fig. 2/S2
E1B	131.979 × 21.402 × 21.402	10 728	216	Fig. 2/S2
E1C	178.350 × 21.402 × 21.402	14 472	216	Fig. 2/S2
E2A	89.175 × 24.969 × 24.969	9898	294	Figure S3
E2B	131.979 × 24.969 × 24.969	14 602	294	Figure S3
E2C	178.35 × 24.969 × 24.969	19 698	294	Figure S3
E3A	89.175 × 28.536 × 28.536	12 928	384	Figure S4
E3B	131.979 × 28.536 × 28.536	19 072	384	Figure S4
E3C	178.350 × 28.536 × 28.536	25 728	384	Figure S4
S1	35.670 × 71.340 × 28.536	13 120	960	Figure S5
S2	35.670 × 71.340 × 71.340	32 800	2400	Figure S5

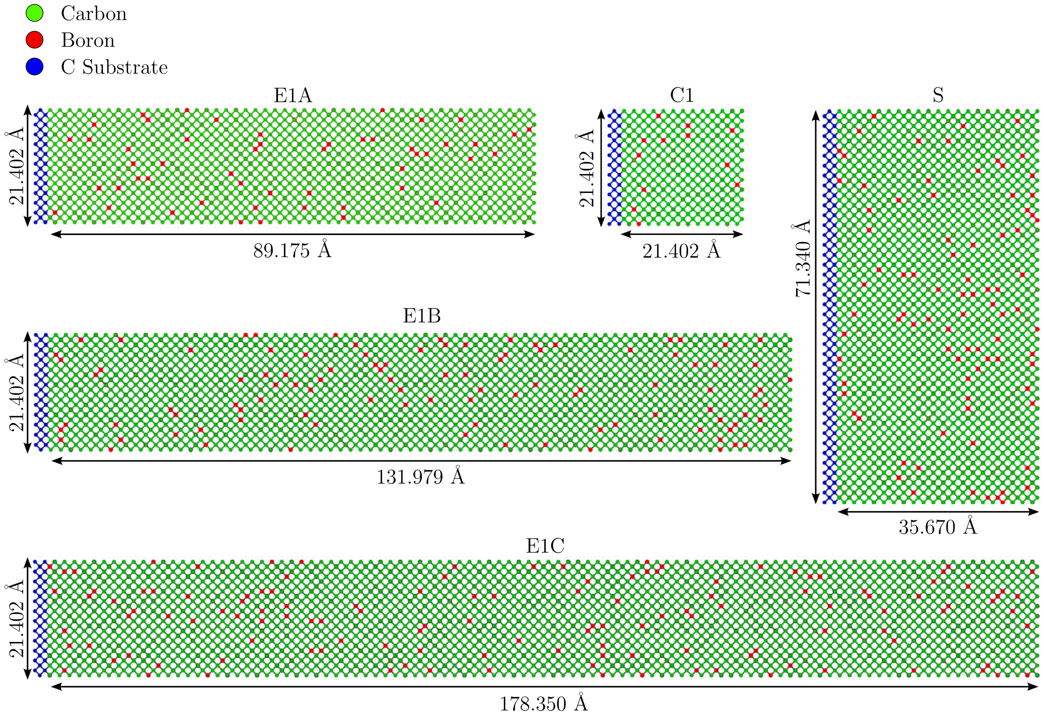

Fig. 2. Representative diagrams of selected crystal structures used in this study, including the cubic crystal C1, slab crystals S1 and S2, and extended crystals E1 A, E1B, and E1C. Carbon atoms are shown in green, boron dopants in red, and substrate carbon atoms in blue. Each structure shows a random dopant distribution corresponding to a boron concentration of $x = 0.05$ (5%). The complete set of crystal structures listed in Table 2 is provided in the SI.

allowing the lateral size to be optimised. The axial dimension was treated differently due to the use of non-periodic boundary conditions along this axis. The lateral dimensions were then kept fixed while L_X was varied to determine whether the crystal structure is sensitive to axial length. In all cases, the lateral dimensions were chosen as integer multiples of the diamond lattice constant, 3.5669 ± 0.0001 Å [51], to make the system fully periodic laterally, effectively simulating a laterally infinite structure.

The resulting crystals fall into three categories: *cubic* crystals, where $L_X = L_Y = L_Z$; *extended* crystals, where $L_Y = L_Z < L_X$; and *slab* crystals, where $L_Y > L_X$ and $L_Z > L_X$. The lateral dimensions are always equal and take one of three values: 21.402 Å, 24.969 Å, or 28.536 Å (equivalent to 6, 7, and 8 unit cells). Three axial dimensions were used: 89.175 Å, 131.979 Å, and 178.350 Å (equivalent to 25, 37, and 50 unit cells). To systematically label these configurations, the following nomenclature is used: *C* for cubic, *E* for extended, and *S* for slab, followed by a numerical index indicating the lateral dimensions: *1* for 21.402 Å, *2* for 24.969 Å, and *3* for 28.536 Å. For E-category crystals, an additional letter denotes the axial length: *A* for 89.175 Å, *B* for 131.979 Å, and *C* for 178.350 Å. In S-category crystals, the numerical index distinguishes $L_Y > L_Z$ (*1*) from $L_Z = L_Y$ (*2*), with a single axial length being used in both cases. The complete set of configurations is listed in Table 2, and representative examples are shown in Fig. 2. Visualisations of all crystal sizes are provided in the SI.

For each dopant concentration, between 50 and 200 unique crystalline structures were generated, each featuring a unique distribution of boron atoms. The number of structures generated was limited by the available CPU time; smaller crystal sizes, being faster to simulate, allowed for more statistical repeats. The total number of simulations for each crystal size is listed in the SI. Generating multiple unique dopant distributions provides a robust and statistically meaningful analysis. All structures initially underwent geometry optimisation using the MBN Explorer velocity quenching algorithm over 10 000 optimisation steps, ensuring that each crystal reached a local energy minimum. This was performed with the simulation box dimensions L_X, L_Y, and L_Z held fixed, such that only atomic positions were relaxed and no optimisation of the lattice or simulation box dimensions was performed. These optimised configurations were used as initial geometries for MD simulations, which were conducted at 300 K using a Langevin thermostat with a damping time of 0.2 ps for a period of 1 ns. This process allowed for full thermalisation of the system within the canonical (NVT) ensemble, with the number of particles, simulation volume, and temperature kept constant throughout. It should be noted that this approach neglects temperature gradients that are present during MPCVD growth; however, such gradients primarily affect the growth kinetics, and can lead to the formation of defect. This simplifying assumption may lead to underestimations of the lattice distortion, and therefore the simulations represent the idealised, post-growth equilibrium properties of the crystal.

The crystal generation methodology described here offers three advantages: (i) it enables the use of periodic boundary conditions to simulate an effectively infinite crystal while maintaining a manageable number of atoms; (ii) it eliminates the majority of edge effects observed in our previous $Si_{1-x}Ge_x$ study [44]; (iii) it enables the analysis of structural behaviour in different regions of the crystal. The system is divided into three zones based on distance from the fixed substrate: (i) the region adjacent to the substrate, where mechanical support is strongest; (ii) the central “bulk-like” region, distant from direct constraint; and (iii) the free surface region, where atoms are free to expand into vacuum at the top of the simulation box. These are shown in Fig. 1. Separate analysis of each of these regions allows the response of the local crystal structure to dopant atoms to be assessed. For structural analysis, the final ten frames of each trajectory, corresponding to the last 10 ps, were averaged to account for thermal vibrations. This timescale was chosen to capture multiple vibration periods while excluding larger-scale structural changes occurring over longer durations. Atoms belonging to the fixed substrate were excluded from all analyses.

2.2. Geometric correction

The use of periodic boundary conditions introduces limitations when comparing simulation results with empirical models of dopant-induced lattice expansion, such as Vegard’s Law [52], which predicts a linear relationship between lattice constant and dopant concentration for alloys of identical crystal structure. Vegard’s Law assumes isotropic three-dimensional expansion, whereas the systems here exhibit anisotropic behaviour: expansion in the Y and Z directions is suppressed by the periodic boundaries, while expansion is permitted only along the positive X direction and constrained by the fixed substrate along the negative X direction. The system therefore undergoes effectively one-dimensional expansion. This anisotropy does not influence the analysis of the (1 0 0) inter-planar distances but alters that of the (1 1 0) planes. To enable meaningful comparison with Vegard’s Law and experimental data, a geometric correction must be applied to account for the restricted lateral expansion.

The distance between the crystalline planes $(i\ j\ k)$ may be denoted as d_{ijk}. In an isotropically expanding crystal, the distance between neighbouring (1 1 0) planes, d_{110}, is related to that of the (1 0 0) and (0 1 0) planes (d_{100} and d_{010}, respectively). Since $d_{100} \equiv d_{010}$ in isotropic geometry, we obtain $d_{110} = \sqrt{d_{100}^2 + d_{010}^2} = \sqrt{2} d_{100}$.

In anisotropic geometry, d_{010} remains fixed, while d_{100} increases by a small amount ΔX. The expanded inter-planar distance is denoted by $\tilde{d}_{ijk}$, such that $\tilde{d}_{100} = d_{100} + \Delta X$, with $d_{100} \gg \Delta X$. Therefore, the isotropic and anisotropic expansion of the (1 1 0) planes, $\tilde{d}_{110,i}$ and $\tilde{d}_{110,a}$, are given by:

$$\tilde{d}_{110,i} = \sqrt{2}(d_{100} + \Delta X) \tag{1}$$

$$\tilde{d}_{110,a} = \sqrt{(d_{100} + \Delta X)^2 + d_{010}^2} \approx \tilde{d}_{110,i} \left(1 - \frac{\Delta X}{2 d_{100}}\right) \tag{2}$$

Using these, a geometric correction factor C, which rescales the anisotropic expansion to reflect the isotropic scenario, can be obtained:

$$C = \frac{\tilde{d}_{110,i}}{\tilde{d}_{110,a}} \approx 1 + \frac{\Delta X}{2 d_{100}} \tag{3}$$

The values of d_{010} and ΔX are obtained from the simulations. The correction factor C is computed independently for each crystal size, dopant concentration, and spatial region, and is applied by multiplying the determined d_{110} by the corresponding C. While this approach substantially reduces the bias associated with constrained expansion, it does not account for cases in which multiple crystal facets such as (1 1 0) and (1 1 1) contribute simultaneously to the overall strain response.

3. Results and discussion

In this section, the structural properties of $C_{1-x}B_x$ crystals are analysed, including the lattice constant and inter-planar distances as functions of boron concentration.

3.1. Overview of structural metrics

The nominal values for the diamond lattice constant a_C and the inter-planar spacings used here are 3.5669 ± 0.0001 Å [51] for a_C, 1.2611 Å for d_{110}, and 0.8917 Å for d_{100} at 300 K. Due to the cubic structure of the crystals, the lattice constant is equal in all crystallographic directions. The d_{110} inter-planar distances are of most interest in this work, as it is through these planes that particles channel in CLSs; see Fig. 1. In comparison, the d_{100} inter-planar distances provide a measure of the axial expansion or contraction.

Inter-planar distances were determined by projecting all atoms onto the $(1, 1, 0)$ and $(1, 0, 0)$ planes. Atoms belonging to each plane were grouped, and the plane positions were defined as the average coordinates of their constituent atoms. Inter-planar distances were calculated as the separation between successive plane positions and averaged over all planes of the same type within each crystal, yielding characteristic d_{110} and d_{100} values. To obtain statistically representative values, ensemble averages across all crystals of a given size and dopant concentration were taken. Relative changes in lattice constant and inter-planar distance, $\Delta a_{CB}/a_C$, $\Delta d_{110}/d_{110}$, and $\Delta d_{100}/d_{100}$, were also calculated, as these quantities are widely reported in the context of lattice expansion and crystal characterisation [8,39].

Vegard’s Law [52] provides a useful point of comparison for the calculated lattice constants and inter-planar distances. This empirical relationship predicts a linear dependence of the lattice constant a_{AB} on the dopant concentration x for binary systems composed of two components, A and B, that share the same crystalline structure, and is given by Eq. (4). For $C_{1-x}B_x$ systems, its direct application is complicated by the fact that elemental boron does not naturally crystallise into a stable cubic structure. At room temperature, boron is most stable in the β-rhombohedral phase [53]. In BDD, however, boron atoms act as substitutional impurities occupying carbon lattice sites. As a result, the lattice constant a_B required for Eq. (4) cannot be defined in the same way as for conventional substitutional alloys such as $Si_{1-x}Ge_x$. To address this limitation, two modifications have been proposed: one based on covalent radii [39] and another on atomic volumes [54]. Both take the simplified form of Eq. (5):

$$a_{AB} = (1 - x) a_A + a_B x \tag{4}$$

$$a_{CB} = a_C(\kappa x + 1) \tag{5}$$

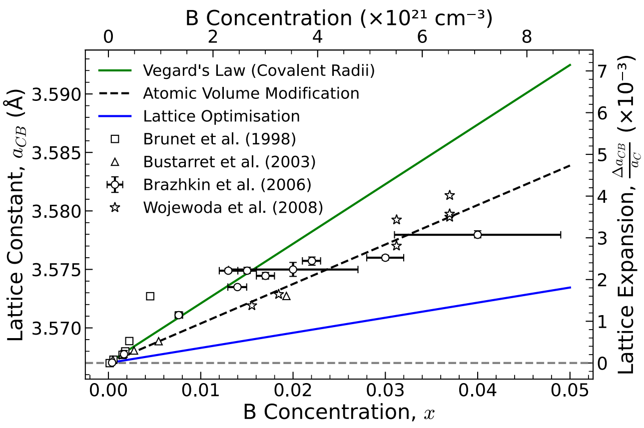

Fig. 3. Compilation of literature data showing the lattice constant a_{CB} and relative lattice expansion $\Delta a_{\mathrm{CB}}/a_{\mathrm{C}}$ of $\mathrm{C}_{1-x}\mathrm{B}_x$ crystals as a function of boron concentration x. The solid green line represents the covalent radius modification to Vegard's Law [39], while the dashed black line shows the atomic volume modification Ref. [54]. The solid blue line shows the results of lattice optimisation, which are discussed in Section 3.2, but presented here as a point of comparison. Comparison data are taken from multiple sources including experimental works from Ref. [39] (open squares), Ref. [55] (open triangles), and Ref. [54] (open circles), and *ab initio* calculations from Ref. [56] (open stars).

where κ is a coefficient determined by the chosen modification, x is the fractional concentration of boron, and a_{C} is the lattice constant of pure diamond. The covalent radii of carbon and boron ($r_{\mathrm{C}} = 0.77$ Å and $r_{\mathrm{B}} = 0.88$ Å [37]) are used to determine the coefficient κ_r (see below), which is adopted here as the reference form of Vegard's Law for $\mathrm{C}_{1-x}\mathrm{B}_x$ systems. The atomic volumes $V_{\mathrm{C}} = 5.67\,\text{Å}^3$/atom [37] for diamond and $V_{\mathrm{B}} = 7.28\,\text{Å}^3$/atom[1] Ref. [54], derived from crystallographic measurements of unit cell volumes and densities, are used to determine κ_V:

$$\kappa = \begin{cases} \kappa_r = 0.14286 & \text{(covalent radii)} \\ \kappa_V = 0.09465 & \text{(atomic volumes)} \end{cases} \tag{6}$$

These relationships are shown in Fig. 3, with the green line representing the covalent radius modification, and the black dashed line the atomic volume modification, together with experimental data [39,54,55] and computational results [56]. The large uncertainties in dopant concentration reported by Ref. [54] are not explained, but are likely the result of measurement uncertainties in the methods used to estimate the boron concentration of their samples. It is evident from this plot that the atomic volume modification provides a better estimate of the lattice expansion at higher dopant concentrations ($x \gtrsim 0.015$), though both relationships are valid at low dopant concentrations ($x \lesssim 0.005$).

Although widely used, the atomic-volume modification raises questions: it appears to rely on the atomic volume of β-rhombohedral boron[1]– whose structure differs fundamentally from cubic diamond – yet the precise method is not specified. Ref. [56] instead proposed a three-component relationship based on covalent radii, the fraction of boron atoms forming B–B pairs (B_2 dimers), and the concentration of free charge carriers:

$$a_{CB} = a_C(\kappa_r x + \kappa_{\mathrm{pair}} x_{BB} + \kappa_f x + 1), \tag{7}$$

where $\kappa_{\mathrm{pair}} = 0.021824$ is a coefficient accounting for the presence of B_2 dimers (derived from *ab initio* calculations), x_{BB} is the fraction of B_2, and $\kappa_f = \kappa_V - \kappa_r = -0.04821$ is the free-carrier coefficient, evaluated using the values in Eq. (6). This relationship is exactly equivalent to the atomic-volume modification derived by Ref. [54] and is therefore omitted from Fig. 3 for clarity.

Since Vegard's Law assumes isotropic, linear expansion, the inter-planar distances are expected to scale proportionally. The relation in Eq. (5) can therefore be applied to d_{ijk} by substituting $a_{\mathrm{CB}} \rightarrow d_{\mathrm{CB}}$ and $a_{\mathrm{C}} \rightarrow d_{\mathrm{C}}$, where d_{C} denotes the inter-planar spacing in pure diamond for a given crystalline plane. As both lattice constants and inter-planar distances scale linearly, the relative change $\Delta d_{ijk}/d_{ijk}$ is equivalent to $\Delta a_{CB}/a_{\mathrm{C}}$.

3.2. *Variation of lattice constants*

The lattice constant was calculated directly from the atomic coordinates of the thermalised systems after MD simulations. The variation in the lattice constant with dopant concentration is shown in Fig. 4a. Due to the large number of crystal geometries considered in this work, a shaded region is used to represent the full range of results across all crystal sizes at each boron concentration, rather than plotting each individual line. This approach is also used in later sections to present similar results involving many geometries. The complete data sets for all individual geometries are provided in the SI. The nominal lattice constant of pure diamond, the covalent-radius and atomic-volume modifications, and the experimental and computational data are compiled from Fig. 3. The results show a consistent linear trend, in line with expectations from Vegard's Law, reaching a relative lattice expansion of $\Delta a_{\mathrm{CB}}/a_{\mathrm{C}} \sim 2.5 \times 10^{-3}$ across all sizes at a dopant concentration of 5%. Although the data points have associated boron-concentration uncertainties, these have been omitted from the plots for clarity. The error bars on both axes are small and are provided explicitly in the SI.

Compared to the covalent radius and atomic volume modifications, and with literature data, discrepancies are clearly evident. However, at low dopant concentrations (below $\sim 0.5\%$), there is reasonably good agreement between the simulation results and literature data, as seen in the zoomed-in view in Fig. 4b. It is exactly these low levels of boron doping that are of most interest for the manufacture of gamma-ray CLS crystals, with candidate crystals manufactured to date not exceeding $\sim 1\%$ of B [8,9]. A slight deviation from the nominal value of the lattice constant is also observed, which may be attributed to edge effects that occur in the free-edge region of the crystal. While the area most affected has been excluded from analysis, these effects still propagate into the overall structure.

Across the full range of dopant concentrations considered, the lattice constant remains linear with concentration, consistent with the behaviour predicted by Vegard's Law. However, the slope of this linear relationship is systematically lower than Vegard's Law predicts. At higher dopant concentrations, a significant deviation from the atomic volume modification and literature data is observed. This deviation can be quantified by fitting simulation results to Eq. (5) to obtain an average value of $\kappa_{\mathrm{MD}} \approx 0.05093$ across all crystal sizes. It should be noted that such deviations are well documented for $\mathrm{C}_{1-x}\mathrm{B}_x$ crystals [39,55–57] and for other materials [58], although not to the extent observed in our simulations. This deviation may arise for several reasons. The first concerns the structural quality of the crystals used in this work. The methods herein utilised generate crystals very close to the ideal diamond structure, with direct, random substitution of boron atoms. In contrast, experimental methods such as MPCVD grow crystals layer by layer, introducing boron via the gas phase [8,38,39]. The chemical and kinetic processes associated with this growth and incorporation can inherently lead to the formation of point defects, such as dopant atom clusters, vacancies, atoms located at interstitial positions, as well as dislocations, and residual stresses, all of which can alter the effective lattice parameter and structure. This represents a fundamental limitation of the methodology implemented in this work, and thus the results must be considered to show the equilibrium structural properties of the system at the upper bound of crystal quality.

---

[1] The origin of this value is not specified in Ref. [54], but it is most likely derived from the density of β-rhombohedral boron.

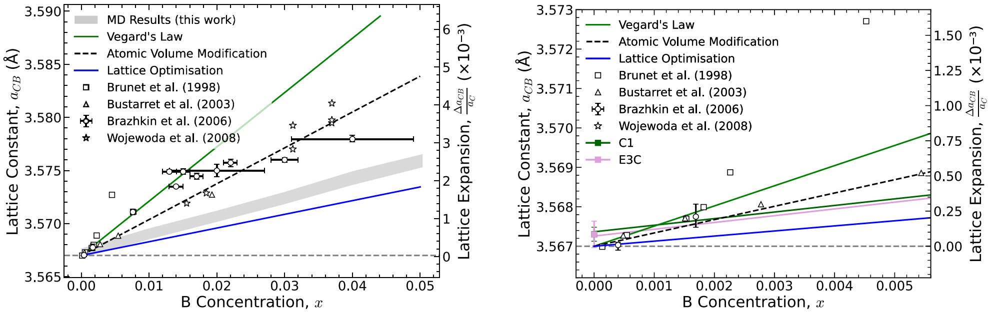

(a) (b)

Fig. 4. Plots of the lattice constant a_{CB} as a function of boron dopant concentration. The grey shaded region in panel **(a)** spans the full range of values obtained across all crystal sizes listed in Table 2. Lines corresponding to individual crystal sizes are available in the SI. The solid green line corresponds to Vegard's Law [39], while the dashed black line represents the atomic volume modification [54]. The dashed grey line indicates the nominal lattice constant of pure diamond. Comparison data are taken from multiple sources including experimental works from Ref. [39] (open squares), Ref. [55] (open triangles), and Ref. [54] (open circles), and *ab initio* calculations from Ref. [56] (open stars). Panel **(b)** shows a zoom in on lower concentrations and shows only the two extreme cases (C1 and E3C) to allow easier differentiation between the two lines.

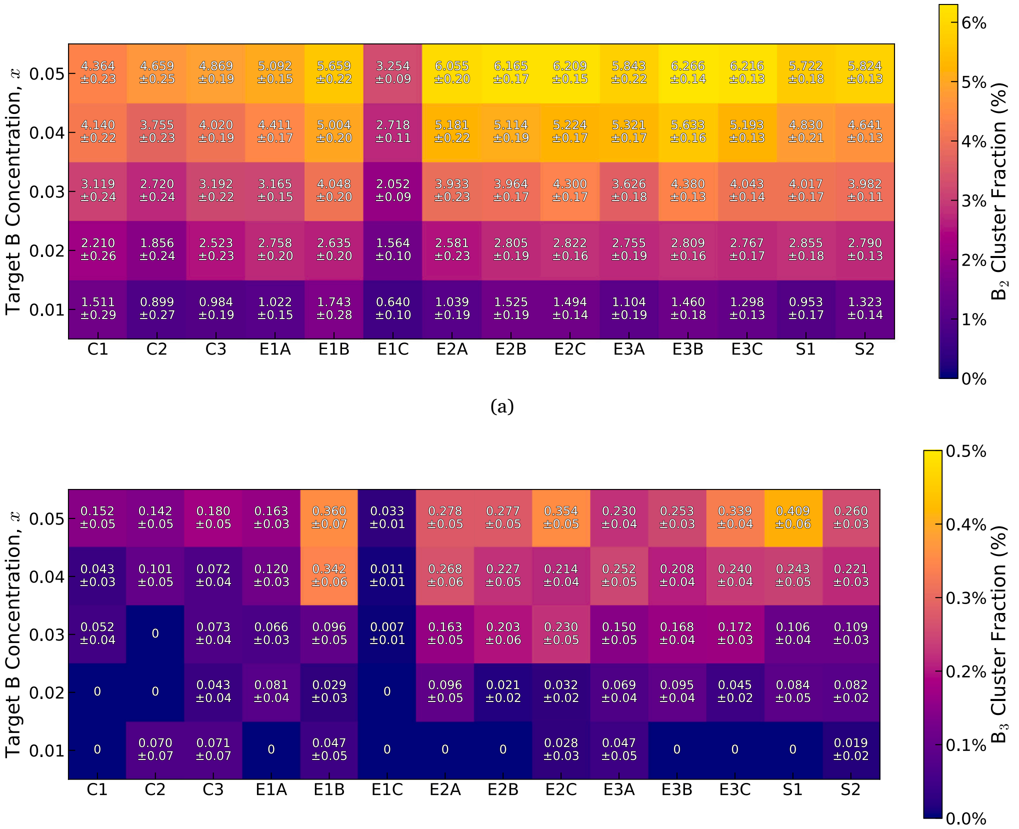

	C1	C2	C3	E1A	E1B	E1C	E2A	E2B	E2C	E3A	E3B	E3C	S1	S2
0.05	4.364 ±0.23	4.659 ±0.25	4.869 ±0.19	5.092 ±0.15	5.659 ±0.22	3.254 ±0.09	6.055 ±0.20	6.165 ±0.17	6.209 ±0.15	5.843 ±0.22	6.266 ±0.14	6.216 ±0.13	5.722 ±0.18	5.824 ±0.13
0.04	4.140 ±0.22	3.755 ±0.23	4.020 ±0.19	4.411 ±0.17	5.004 ±0.20	2.718 ±0.11	5.181 ±0.22	5.114 ±0.19	5.224 ±0.17	5.321 ±0.17	5.633 ±0.16	5.193 ±0.13	4.830 ±0.21	4.641 ±0.13
0.03	3.119 ±0.24	2.720 ±0.24	3.192 ±0.22	3.165 ±0.15	4.048 ±0.20	2.052 ±0.09	3.933 ±0.23	3.964 ±0.17	4.300 ±0.17	3.626 ±0.18	4.380 ±0.13	4.043 ±0.14	4.017 ±0.17	3.982 ±0.11
0.02	2.210 ±0.26	1.856 ±0.24	2.523 ±0.23	2.758 ±0.20	2.635 ±0.20	1.564 ±0.10	2.581 ±0.23	2.805 ±0.19	2.822 ±0.16	2.755 ±0.19	2.809 ±0.16	2.767 ±0.17	2.855 ±0.18	2.790 ±0.13
0.01	1.511 ±0.29	0.899 ±0.27	0.984 ±0.19	1.022 ±0.15	1.743 ±0.28	0.640 ±0.10	1.039 ±0.19	1.525 ±0.19	1.494 ±0.14	1.104 ±0.19	1.460 ±0.18	1.298 ±0.13	0.953 ±0.17	1.323 ±0.14

(a)

	C1	C2	C3	E1A	E1B	E1C	E2A	E2B	E2C	E3A	E3B	E3C	S1	S2
0.05	0.152 ±0.05	0.142 ±0.05	0.180 ±0.05	0.163 ±0.03	0.360 ±0.07	0.033 ±0.01	0.278 ±0.05	0.277 ±0.05	0.354 ±0.05	0.230 ±0.04	0.253 ±0.03	0.339 ±0.04	0.409 ±0.06	0.260 ±0.03
0.04	0.043 ±0.03	0.101 ±0.05	0.072 ±0.04	0.120 ±0.03	0.342 ±0.06	0.011 ±0.01	0.268 ±0.06	0.227 ±0.05	0.214 ±0.04	0.252 ±0.05	0.208 ±0.04	0.240 ±0.04	0.243 ±0.05	0.221 ±0.03
0.03	0.052 ±0.04	0	0.073 ±0.04	0.066 ±0.03	0.096 ±0.05	0.007 ±0.01	0.163 ±0.05	0.203 ±0.06	0.230 ±0.05	0.150 ±0.05	0.168 ±0.04	0.172 ±0.03	0.106 ±0.04	0.109 ±0.03
0.02	0	0	0.043 ±0.04	0.081 ±0.04	0.029 ±0.03	0	0.096 ±0.05	0.021 ±0.02	0.032 ±0.02	0.069 ±0.04	0.095 ±0.04	0.045 ±0.02	0.084 ±0.05	0.082 ±0.02
0.01	0	0.070 ±0.07	0.071 ±0.07	0	0.047 ±0.05	0	0	0	0.028 ±0.03	0.047 ±0.05	0	0	0	0.019 ±0.02

(b)

Fig. 5. Heatmaps showing the average fraction of B–B atoms pairs **(a)** and B_3 clusters **(b)** relative to isolated B atoms as a function of boron concentration and crystal size. Each box reports the average percentage of B–B atom pairs out of all B atoms for the corresponding crystal size and dopant concentration.

Another possible origin of the discrepancy observed in Fig. 4 is the formation of boron clusters. The three-component form of Vegard's Law [56] given in Eq. (7) explicitly accounts for contributions from B_2 dimers. At higher boron concentrations, the formation of B_2 and larger clusters (B_3 and B_4) becomes energetically favourable and has been shown to impact the overall lattice structure [56,59]. Incorporation of these clusters leads to lattice expansion due to the larger covalent radius of boron. Figs. 5a and b show heatmaps of the fractions of boron atoms found in B_2 and B_3 clusters, compared to isolated dopants, as functions of concentration and crystal size. The fraction of B_2 clusters increases with dopant concentration, as expected, but remains uniform across crystal sizes. An exception is the C-category crystals which show a lower fraction of B_2 compared to the larger E and S-category crystals, most likely due to the smaller overall number of atoms in these systems

Overall, the proportion of B_2 clusters observed in the simulation results is very small: at 5% doping, at most $\sim$ 6.2% of all boron atoms exist in B_2 clusters, corresponding to just $\sim$ 0.31% of all atoms in the crystal. This low cluster fraction likely reflects the small system sizes relative to experimental MPCVD-grown crystals. To our knowledge, no experimental study has quantitatively measured B_2 (or larger) clusters in MPCVD-grown crystals; nevertheless, clustering is expected, with several studies suggesting significant B_2 dimer formation [60–63], and Ref. [59] explicitly stating that "a significant fraction of boron atoms may form B dimers". Thus, while present in the crystals analysed in this work, the impact of B_2 clusters is likely negligible.

A similar analysis of B_3 clusters (Fig. 5b) shows a much lower concentration than for B_2, with similar trends: a higher fraction of B_3 clusters in larger E- and S-category crystals at concentrations above $x = 0.03$, and almost none in C-category crystals. Analyses of B_4 clusters were also conducted; however, across the 1940 unique crystal structures generated here, only 17 B_4 clusters were identified, compared with 674 B_3 and 3444 B_2 clusters. No clusters larger than B_4 were found. This extremely low prevalence of boron clusters provides further evidence of the high-quality crystal structures generated by the present methodology and may, in part, explain the deviation from Vegard's Law observed. As emphasised in Section 1, such high-quality, defect-free crystals are essential for gamma-ray CLS applications, while defect characterisation in MPCVD-grown crystals remains an active topic [7,11]. Based on the computational methodology used, the lack of dopant clusters is not necessarily unexpected. As previously discussed, the dopant methodology of random substitution employed here is representative of a equilibrium structure, and neglects the consideration of the growth kinetics associated with the MPCVD fabrication process. MPCVD permits cluster formation from surface diffusion of deposited atoms, allowing for both the formation of clusters and lattice vacancies. However, these processes take place over timescales much longer, and temperatures much higher than modelled here.

The three-component model of Eq. (7) [56] also accounts for the influence of free carriers on the lattice: boron doping leads to free holes, thereby rendering the material a p-type semiconductor. These free carriers induce a negative lattice strain via hydrostatic deformation of the valence-band maximum, as quantified by Ref. [56], leading to a negative deviation from Vegard's Law at higher dopant concentrations. The MD simulations conducted here do not capture such electronic (valence-band) effects; instead, the predicted lattice expansion arises solely from steric effects associated with substitutional boron. While this represents a limitation of the method, it is of minor consequence for this work, which focuses on evaluating the structural influence of dopant atoms to inform crystal fabrication.

As a final test, lattice optimisation simulations were performed. In MD simulations, crystals were initially generated with the experimental lattice constant of diamond, $a_C = (3.5669 \pm 0.0001)\,\text{Å}$ [51]. Lattice optimisation of pure diamond yielded an optimised lattice constant of $3.561\,\text{Å}$. Corresponding lattice optimisation of a cubic boron crystal constructed by replacing all carbon atoms with boron yielded a lattice constant of $3.690\,\text{Å}$. Using these values with Vegard's Law, Eq. (4), results in a slightly smaller slope than obtained from our MD simulations ($\kappa_{MD} \approx 0.05093$), with $\kappa_{opt} = 0.03623$. These results are shown as the blue line in Figs. 3 and 4a. Atomic volumes calculated from the optimised structures are $V_C = 5.64\,\text{Å}^3/\text{atom}$ and $V_B = 6.28\,\text{Å}^3/\text{atom}$. While the diamond volume closely matches literature values [37], the cubic boron volume is lower than that of β-rhombohedral boron. Using these volumes to calculate κ_V gives $\kappa_V = 0.03760$, consistent with the κ_{opt}. Lattice optimisation simulations are conducted without a thermostat, so thermal effects are not included. Accounting for thermal expansion would increase the optimised lattice constants, owing to the increased thermal expansion of boron compared to diamond ($\sim 6 \times 10^{-6}\,\text{K}^{-1}$ [64] vs $\sim 1 \times 10^{-6}\,\text{K}^{-1}$ [65]), reducing the difference relative to the MD simulation results. These lattice optimisation results are more in line with the results of MD simulations, and suggest that the atomic volume for boron quoted by Ref. [54][1] leads to an overestimation in the lattice constant by the atomic volume modification. This warrants further investigation and may form the focus of a future study.

Taken together, a combination of enhanced crystal quality, negligible B_2 clustering, and overestimation of the atomic volume of boron in comparison to the results of lattice optimisation provides a reasonable explanation for the discrepancy observed between the results of MD simulations and results from literature.

3.3. Variation of inter-planar distances

Building on the analysis of lattice constants, the influence of boron doping on inter-planar distances can be investigated across the three spatial regions outlined in Section 2. The boundaries between these regions are shown in Fig. 1, and were defined based on a fixed number of atomic layers measured along the [1 0 0] direction, from the variation in (1 0 0) inter-planar distance as a function of the distance from the substrate. For consistency, the same boundary positions were used across all crystal sizes: seven atoms thick for the substrate region (excluding the fixed substrate), and ten atoms thick for the free edge. More details describing the method by which these regions were defined is available in the SI.

The variation in (1 1 0) and (1 0 0) inter-planar distances with boron dopant concentration are shown in Figs. 6a and b, respectively, with the grey shaded regions representing the full range of values obtained for the bulk region across all crystal sizes. The complete set of plots for all crystal sizes and spatial regions is provided in the SI, and is summarised later in this section. To facilitate comparison between crystal sizes, Fig. 7 shows the (1 1 0) and (1 0 0) inter-planar distances for each region, where each point represents the average over all sizes within the corresponding major crystal category (C, E1, E2, E3, or S). In all cases a dopant concentration of $x = 0.01$, which is most representative of gamma-ray CLS crystals, is used. A corresponding plot showing all individual crystal sizes listed in Table 2 can be seen in Figure S13 of the SI.

3.3.1. Substrate region

As outlined in Section 2, the crystal generation method includes a three-atom-thick fixed diamond layer to mimic the supportive role of the substrate typically used in CVD crystal growth. The size of this region was fixed at seven atomic layers from the fixed substrate, independent of the overall crystal size. This consistent definition enables a direct comparison of the influence of bulk region size and substrate anchoring on inter-planar distances.

In the substrate region, the inter-planar distances between the (1 1 0) and (1 0 0) planes are broadly similar, as can be seen in Fig. 7 (and Figure S13 in the SI) which show similar values for all crystal sizes and for both plane sets. This is particularly the case for the C-category crystals, where simulation statistics are highest and thus the error bars in Fig. 7 are smallest. Larger crystals (E1 and E2) show slight variation between inter-category sizes, as seen from the larger statistical error bars and directly from Figure S13. These, however, largely remain within these statistical error bars and are therefore not considered significant. Overall, these observations indicate that the substrate is playing a supportive role in constraining this region for both the (1 1 0) and (1 0 0) crystalline planes.

3.3.2. Bulk region

The bulk region constitutes the central portion of the crystal, surrounded by atoms on all sides: laterally through the periodic boundaries, and axially by the substrate and free-edge regions. As such, this configuration effectively emulates the interior of an infinitely periodic crystal. The extent of the bulk region does not correspond to a fixed number of atomic layers, but is defined by the volume not occupied by the substrate or free edge. Therefore, the number of atomic layers in this region varies from a minimum of 8 for the smallest crystal (C1) up to 184 for the largest one (E3C).

The bulk region exhibits a greater dependence on the axial crystal dimension compared to the substrate region. The full plots showing

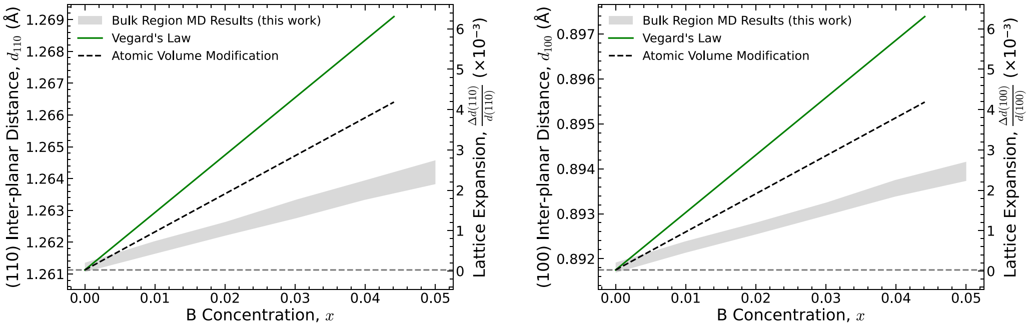

(a)

(b)

Fig. 6. (1 1 0) and (1 0 0) inter-planar distances (panels **(a)** and **(b)** respectively) as a function of boron dopant concentration. The grey shaded regions represents the full range of values obtained for the bulk region across all crystal sizes. Specific cases showing the region-by-region inter-planar distances for individual crystal sizes are available in the SI. The solid green line represents Vegard's Law [52]; the dashed black line shows the atomic volume interpolation correction [54]; and the dashed grey line indicates the nominal inter-planar spacing in pure diamond.

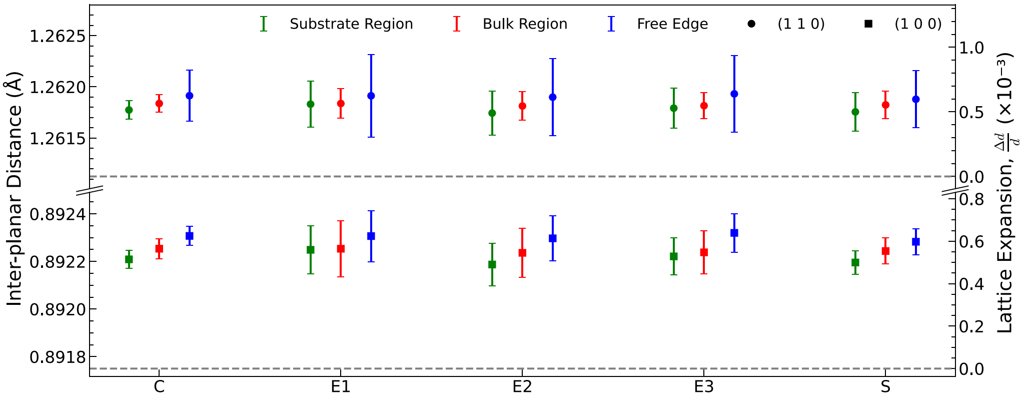

Fig. 7. Calculated values of the (1 1 0) (circles) and (1 0 0) (squares) inter-planar distances across the major crystal categories C, E1, E2, E3, and S. Each point represents the average over all crystal sizes within the corresponding category and is shown for each spatial region of the crystal: substrate (green), bulk (red), and free edge (blue). A corresponding plot showing results for each individual crystal size listed in Table 2 is provided in Figure S13 of the SI.

dependences for individual crystal sizes provided in Section S4 of the SI show a systematic increase in the (1 1 0) inter-planar distances as the axial dimensions of the crystal increase. This behaviour is most pronounced at higher dopant concentrations but is still observed across most crystal categories at $x = 0.01$. This can also be seen in a direct comparison of Fig. 6a and b, where the shaded region representing the full range of bulk region values across all crystal sizes is wider for the (1 1 0) inter-planar distances than for the (1 0 0) inter-planar distances. This can also be directly observed from the red points in Figure S13. The only exception is the S-category, where the axial dimensions are the same for S1 and S2. This effect is not observed for the (1 0 0) planes, where the inter-planar distances remain uniform across all crystal sizes.

This dependence of the (1 1 0) planes on axial dimensions may be attributed to bulk-size effects: at smaller sizes the crystals do not occupy a sufficiently bulk-like volume, so finite-size effects yield smaller increases in inter-planar distance. This effect is most pronounced along the axial direction, as this is the direction of expansion, and the (1 1 0) inter-planar distances have components from both the X direction expansion, and the fixed Y direction. In comparison, for the (1 0 0) planes, there is only a single expansion component, so the limited expansion of the crystal in the Y and Z directions does not play a role. In short, this is a geometric artefact arising from the anisotropic expansion of the system, even after applying the geometric correction, and it provides further evidence that the substrate plays a supportive role in the substrate region.

3.3.3. *Free edge*

The free-edge region is the portion of the crystal that is exposed to vacuum. It is initially defined to include the ten atomic layers adjacent to the free edge. Of these, the three layers closest to the surface are excluded from analysis due to atypical coordination and geometry arising from the absence of periodic boundaries along the [1 0 0] direction. This leaves seven atomic layers included in the analysis, matching the number used for the substrate region.

In this region, the absence of periodic support along X leads to surface relaxation and edge effects, producing large crystal-to-crystal deviations in inter-planar distance, even between crystals of the same size and dopant concentration. A deviation from the nominal inter-planar distance is evident from the non-zero width of the shaded region in the undoped case in Figs. 6a and b, directly resulting from these edge effects. Similar behaviour is observed for the lattice constant in Fig. 4b and, to a lesser extent, in the bulk and substrate regions. Although an overall linear dependence is present here, the associated uncertainties are substantially larger. The (1 1 0) and (1 0 0) planes show comparable variability across all crystal sizes (blue points in Fig. 7), and this region consistently exhibits the largest inter-planar distances. In general, there is no distinct size trend, although the S-category crystals show the least variation across sizes from Figure S13. This most likely reflects their larger unconstrained surface (greater Y and Z dimensions), which provides more atoms in the averaging region and thus better statistics. Overall, a free surface permits larger local relaxations that depart from bulk behaviour, as expected. The diamond

(1 0 0) surface is also known to undergo a 2 × 1 dimer reconstruction to reduce the energy associated with dangling bonds [66,67], which is not explicitly modelled in these simulations. This relaxation mainly affects the few atomic layers closest to the surface, thus the absence of explicit surface reconstruction is not expected to significantly influence the lattice expansion in this region.

Results in this region should be treated with caution, as the uncertainties are inherently large. We include the free-edge results for completeness and as a methodological demonstration, but the analysis of this region is not exhaustive; a fuller understanding would require further work beyond the scope of this study.

4. Conclusions and outlook

In this study, atomistic-scale molecular dynamics simulations were performed on a range of periodically replicated $C_{1-x}B_x$ crystals with boron concentrations between $x = 0.00$ and $x = 0.05$. The aim was to elucidate the effects of boron atom substitution on the lattice structure for crystals of various sizes. These simulations have been conducted in the context of the design and practical realisation of crystal-based gamma-ray light sources based on periodically bent crystals. Given that the performance of such crystals depends on precise structural control, particularly regarding dopant incorporation, a detailed understanding of the effects of boron concentration is essential for establishing practical manufacturing tolerances.

A clear linear relationship has been observed between boron concentration and both the lattice constant and the inter-planar distances of the (1 1 0) and (1 0 0) planes across all crystal sizes studied. By dividing the simulation box into three distinct regions (substrate-adjacent, bulk, and free edge), the response of distinct structural environments to boron doping has been analysed. Across all crystal sizes, the lattice constant follows the same linear dependence, with only minor variations that fall within evaluated error bars. In the substrate region, the inter-planar distance remains essentially uniform across all crystal sizes, confirming the mechanical support provided by the fixed substrate. In contrast, the bulk region exhibits a geometric dependence with increasing axial crystal dimension on the (1 1 0) inter-planar distance. This may be attributed to the finite size effects of the crystal and artifacts originating from the anisotropic nature of the expansion in the simulations. At the free edge, increased variability in the inter-planar distances is observed, attributed to edge effects caused by the absence of periodic support.

Across all regions, the results consistently deviate from the predictions of the covalent radius [39] and atomic volume [54] modifications to Vegard's Law [52], and other literature data [39,54–56]. This deviation may be attributed to several factors, including enhanced crystal quality relative to MPCVD-grown crystals: the methodology presented here yields near-ideal structures in which boron atoms directly substitute for carbon, and interstitial atoms are excluded. By comparison, MPCVD growth is not expected to produce purely substitutional boron but rather an alloy-like structure with clusters, interstitial atoms, and defects. Indeed, our simulations show only a very small fraction of boron clusters, which may also contribute to the discrepancy.

In the context of gamma-ray CLS crystals, a defect-free structure as close to an ideal crystal as possible is desirable. Such high-quality crystals were not the focus of the experimental works of Refs. [39,54,55], where crystal quality was not the main focus, thus a deviation from their results is expected. The results presented here are therefore indicative of an upper-bound case for the design of gamma-ray CLSs. While crystals of such high quality are not currently obtainable in practice, these results therefore serve as a reference for defect-free, stress-free, fully substitutional crystals, providing a clear benchmark for the manufacture of high-quality BDD light-source materials. Indeed, recent reports of near defect-free crystals manufactured for gamma-ray CLS applications [68] suggest that this idealised limit is relevant to the cutting edge of current fabrication techniques.

Another important aspect is the boron concentration. This study considers dopant levels up to 5%, well above those typically used in BDD crystals. At the lower concentrations of $\lesssim 1\%$ typically used in BDD crystal growth, our results show good agreement with other literature data. At higher dopant concentrations less data is available and uncertainties increase due to the formation of defects. The crystal sizes used here are small compared with typical nanometre-scale defects, which therefore cannot be analysed by the present methods. MPCVD could instead be modelled as a stochastic process via kinetic Monte Carlo (kMC) simulations. A number of works have utilised such methods to model CVD growth of diamond [69,70], though to our knowledge boron incorporation has never been explicitly included, and instead only modelled using Density Functional Theory (DFT) [71,72]. Importantly, the work presented here should be viewed as a first step towards more comprehensive modelling of boron-doped diamond systems. Future studies may extend this framework by incorporating additional complexities such as interstitial dopant atoms, periodically graded dopant profiles, and realistic growth processes.

Building upon our earlier work on $Si_{1-x}Ge_x$ systems [44], this study implements an improved simulation framework incorporating both substrate effects and periodic boundary conditions in $C_{1-x}B_x$ crystals, making it more representative of real materials used in gamma-ray CLSs. This methodology offers a computationally efficient and accurate platform not only for studying lattice distortions but also for investigating other material responses relevant to CLS development, such as amorphisation and phase transitions, radiation damage, and thermal effects. Coupled with experimental data, these simulations offer a powerful route for guiding the design of next-generation crystal-based light sources.

CRediT authorship contribution statement

Matthew D. Dickers: Writing – review & editing, Writing – original draft, Visualization, Software, Methodology, Investigation, Formal analysis, Data curation, Conceptualization. **Felipe Fantuzzi:** Writing – review & editing, Supervision. **Nigel J. Mason:** Writing – review & editing, Supervision. **Gennady B. Sushko:** Software, Methodology. **Andrei V. Korol:** Writing – review & editing, Validation, Supervision, Software, Methodology, Conceptualization. **Andrey V. Solov'yov:** Writing – review & editing, Supervision, Software, Methodology, Conceptualization.

Declaration of competing interest

The authors declare that they have no known competing financial interests or personal relationships that could have appeared to influence the work reported in this paper.

Acknowledgements

This work was funded by UK Research and Innovation (UKRI) under the UK government's Horizon Europe funding Guarantee under the grant No. 10037865 in collaboration with the European Commission's Horizon Europe-EIC-Pathfinder-Open TECHNO-CLS (G.A. 101046458) project. The authors also acknowledge financial support from the H2020 RISE-NLIGHT project (G.A. 872196), and from the COST Action CA20129 MultIChem, supported by COST (European Cooperation in Science and Technology). The work was supported in part by Deutsche Forschungsgemeinschaft, Germany (Project No. 413220201). The authors gratefully acknowledge the Specialist and High Performance Computing systems provided by Information Services at the University of Kent. Special thanks are extended to Dr Timothy Kinnear for HPC assistance with the Icarus cluster at the University of Kent. The authors kindly thank the four anonymous referees, whose valuable comments have improved the quality and clarity of this manuscript.

Appendix A. Supplementary data

Supplementary material related to this article can be found online at https://doi.org/10.1016/j.diamond.2026.113714.

Data availability

The datasets generated and/or analysed during the current study are available from the corresponding author upon reasonable request. Data presented in plots of lattice constant and inter-planar distances are tabulated in the supplementary information.

References

[1] K. Muzyka, J. Sun, T.H. Fereja, Y. Lan, W. Zhang, G. Xu, Boron-doped diamond: current progress and challenges in view of electroanalytical applications, Anal. Methods 11 (2019) 397–414, http://dx.doi.org/10.1039/C8AY02197J.

[2] Y. Einaga, Boron-doped diamond electrodes: Fundamentals for electrochemical applications, Acc. Chem. Res. 55 (24) (2022) 3605–3615, http://dx.doi.org/10.1021/acs.accounts.2c00597.

[3] M. Alkahtani, D.K. Zharkov, A.V. Leontyev, A.G. Shmelev, V.G. Nikiforov, P.R. Hemmer, Lightly boron-doped nanodiamonds for quantum sensing applications, Nanomaterials 12 (4) (2022) http://dx.doi.org/10.3390/nano12040601.

[4] S. Bhattacharya, J. Boyd, S. Reichardt, V. Allard, A.H. Talebi, N. Maccaferri, O. Shenderova, A.L. Lereu, L. Wirtz, G. Strangi, R.M. Sankaran, Intervalence plasmons in boron-doped diamond, Nat. Commun. 16 (1) (2025) 444, http://dx.doi.org/10.1038/s41467-024-55353-0.

[5] L. Thaiyotin, T. Phetchakul, S. Cheirsirikul, S. Supadech, UV photodetectors from B-doped diamond film, in: 2000 TENCON Proceedings. Intelligent Systems and Technologies for the New Millennium (Cat. No. 00CH37119), Vol. 3, 2000, pp. 230–233, http://dx.doi.org/10.1109/TENCON.2000.892263.

[6] A.S. Aksenova, A.A. Altuhov, E.V. Ryabeva, V.T. Samosadnyi, V.S. Feshchenko, A.P. Chernyaev, V.A. Shepelev, The investigation of boron-doped diamond absorbance spectrum, J. Phys. Conf. Ser. 798 (1) (2017) 012149, http://dx.doi.org/10.1088/1742-6596/798/1/012149.

[7] A.V. Korol, A.V. Solov'yov, W. Greiner, Channeling and Radiation in Periodically Bent Crystals, Springer, Berlin, Heidelberg, 2014, http://dx.doi.org/10.1007/978-3-642-54933-5.

[8] S.H. Connell, J. Härtwig, A. Masvaure, D. Mavunda, T.N. Tran Thi, Towards a crystal undulator, in: C. Engelbrecht, S. Karataglidis (Eds.), Proceedings of the 59th Annual Conference of the South African Institute of Physics (SAIP2014), University of Johannesburg, Johannesburg, 2015, pp. 169–174, https://events.saip.org.za/event/34/attachments/1143/1398/SAIP2014-169.pdf.

[9] T.N. Tran Thi, J. Morse, D. Caliste, B. Fernandez, D. Eon, J. Härtwig, C. Barbay, C. Mer-Calfati, N. Tranchant, J.C. Arnault, T.A. Lafford, J. Baruchel, Synchrotron bragg diffraction imaging characterization of synthetic diamond crystals for optical and electronic power device applications, J. Appl. Crystallogr. 50 (2) (2017) 561–569, http://dx.doi.org/10.1107/S1600576717003831.

[10] A.V. Korol, A.V. Solov'yov, Crystal-based intensive Gamma-ray light sources, Eur. Phys. J. D. 74 (10) (2020) 201, http://dx.doi.org/10.1140/epjd/e2020-10239-8.

[11] A. Korol, A.V. Solov'yov, Novel Lights Sources Beyond Free Electron Lasers, Springer Nature, Cham, 2022, http://dx.doi.org/10.1007/978-3-031-04282-9.

[12] A.V. Korol, A.V. Solov'yov, Atomistic modeling and characterizaion of light sources based on small-amplitude short-period periodically bent crystals, Nucl. Instrum. Methods Phys. Res. B 537 (2023) 1–13, http://dx.doi.org/10.1016/j.nimb.2023.01.012.

[13] G.B. Sushko, A.V. Korol, A.V. Solov'yov, Extremely brilliant crystal-based light sources, Eur. Phys. J. D. 76 (9) (2022) 166, http://dx.doi.org/10.1140/epjd/s10053-022-00502-7.

[14] J. Lindhard, Influence of crystal lattice on motion of energetic charged particles, Kongel. Dan. Vidensk. Selsk., Mat. -Fys. Medd. 34 (14) (1965) 1–64.

[15] M. Kumakhov, On the theory of electromagnetic radiation of charged particles in a crystal, Phys. Lett. A 57 (1) (1976) 17–18, http://dx.doi.org/10.1016/0375-9601(76)90438-2.

[16] U.I. Uggerhøj, The interaction of relativistic particles with strong crystalline fields, Rev. Modern Phys. 77 (4) (2005) 1131–1171, http://dx.doi.org/10.1103/RevModPhys.77.1131.

[17] A.V. Korol, A.V. Solov'yov, W. Greiner, Photon emission by an ultra-relativistic particle channeling in a periodically bent crystal, Int. J. Mod. Phys. E 08 (01) (1999) 49–100, http://dx.doi.org/10.1142/S0218301399000069.

[18] V. Guidi, L. Lanzoni, A. Mazzolari, G. Martinelli, A. Tralli, Design of a crystalline undulator based on patterning by tensile Si3N4 strips on a Si crystal, Appl. Phys. Lett. 90 (11) (2007) 114107, http://dx.doi.org/10.1063/1.2712510.

[19] V. Guidi, L. Lanzoni, A. Mazzolari, Patterning and modeling of mechanically bent silicon plates deformed through coactive stresses, Thin Solid Films 520 (3) (2011) 1074–1079, http://dx.doi.org/10.1016/j.tsf.2011.09.008.

[20] L. Malagutti, L. Bandiera, F. Bonafè, N. Canale, D. De Salvador, P. Fedeli, J.R. Garrido, V. Guidi, L. Lanzoni, A. Korol, F. Mancarella, R. Negrello, G. Paternò, M. Romagnoni, F. Sgarbossa, A. Solov'yov, A. Sytov, D. Valzani, A. Mazzolari, From simulation to fabrication: Realizing silicon crystalline undulators with silicon nitride stressor layer patterning, Nucl. Instrum. Meth. Phys. Res. A 1076 (2025) 170480, http://dx.doi.org/10.1016/j.nima.2025.170480.

[21] S. Bellucci, S. Bini, V.M. Biryukov, Y.A. Chesnokov, S. Dabagov, G. Giannini, V. Guidi, Y.M. Ivanov, V.I. Kotov, V.A. Maisheev, C. Malagù, G. Martinelli, A.A. Petrunin, V.V. Skorobogatov, M. Stefancich, D. Vincenzi, Experimental study for the feasibility of a crystalline undulator, Phys. Rev. Lett. 90 (3) (2003) 034801, http://dx.doi.org/10.1103/PhysRevLett.90.034801.

[22] V. Guidi, A. Antonini, S. Baricordi, F. Logallo, C. Malagù, E. Milan, A. Ronzoni, M. Stefancich, G. Martinelli, A. Vomiero, Tailoring of silicon crystals for relativistic-particle channeling, Nucl. Instrum. Methods Phys. Res. B 234 (1) (2005) 40–46, http://dx.doi.org/10.1016/j.nimb.2005.01.008.

[23] E. Bagli, L. Bandiera, V. Bellucci, A. Berra, R. Camattari, D. De Salvador, G. Germogli, V. Guidi, L. Lanzoni, D. Lietti, A. Mazzolari, M. Prest, V.V. Tikhomirov, E. Vallazza, Experimental evidence of planar channeling in a periodically bent crystal, Eur. Phys. J. C 74 (10) (2014) 3114, http://dx.doi.org/10.1140/epjc/s10052-014-3114-x.

[24] R. Camattari, G. Paternò, M. Romagnoni, V. Bellucci, A. Mazzolari, V. Guidi, Homogeneous self-standing curved monocrystals, obtained using sand-blasting, to be used as manipulators of hard X-rays and charged particle beams, J. Appl. Crystallogr. 50 (1) (2017) 145–151, http://dx.doi.org/10.1107/S1600576716018768.

[25] P. Balling, J. Esberg, K. Kirsebom, D. Le, U. Uggerhøj, S. Connell, J. Härtwig, F. Masiello, A. Rommeveaux, Bending diamonds by femtosecond laser ablation, Nucl. Instrum. Methods Phys. Res. B 267 (17) (2009) 2952–2957, http://dx.doi.org/10.1016/j.nimb.2009.06.109.

[26] V. Bellucci, R. Camattari, V. Guidi, A. Mazzolari, G. Paternò, G. Mattei, C. Scian, L. Lanzoni, Ion implantation for manufacturing bent and periodically bent crystals, Appl. Phys. Lett. 107 (6) (2015) 064102, http://dx.doi.org/10.1063/1.4928553.

[27] V. Baryshevsky, I. Dubovskaya, A. Grubich, Generation of gamma-quanta by channeled particles in the presence of a variable external field, Phys. Lett. A 77 (1) (1980) 61–64, http://dx.doi.org/10.1016/0375-9601(80)90637-4.

[28] H. Ikezi, Y. Lin-Liu, T. Ohkawa, Channeling radiation in a periodically distorted crystal, Phys. Rev. B 30 (3) (1984) 1567–1569, http://dx.doi.org/10.1103/PhysRevB.30.1567.

[29] G.V. Dedkov, Channeling radiation in a crystal undergoing an action of ultrasonic or electromagnetic waves, Phys. Status Solidi 184 (2) (1994) 535–542, http://dx.doi.org/10.1002/pssb.2221840227.

[30] A.V. Korol, A.V. Solov'yov, W. Greiner, Coherent radiation of an ultrarelativistic charged particle channelled in a periodically bent crystal, J. Phys. G 24 (5) (1998) L45, http://dx.doi.org/10.1088/0954-3899/24/5/001.

[31] W. Wagner, B. Azadegan, H. Buettig, L.S. Grigoryan, A. Mkrtchyan, J. Pawelke, Channeling radiation on quartz stimulated by acoustic waves, Nuovo Cimento C 34 (4) (2011) 133–140, http://dx.doi.org/10.1393/ncc/i2011-10899-4.

[32] K. Kaleris, E. Kaselouris, V. Dimitriou, E. Kaniolakis-Kaloudis, M. Bakarezos, M. Tatarakis, N.A. Papadogiannis, G.B. Sushko, A.V. Korol, A.V. Solov'yov, Narrowband γ-ray radiation generation by acoustically driven crystalline undulators, Phys. Rev. Accel. Beams 28 (2025) 033502, http://dx.doi.org/10.1103/PhysRevAccelBeams.28.033502.

[33] M. Breese, Beam bending using graded composition strained layers, Nucl. Instrum. Methods Phys. Res. B 132 (3) (1997) 540–547, http://dx.doi.org/10.1016/S0168-583X(97)00455-2.

[34] U. Mikkelsen, E. Uggerhøj, A crystalline undulator based on graded composition strained layers in a superlattice, Nucl. Instrum. Methods Phys. Res. B 160 (3) (2000) 435–439, http://dx.doi.org/10.1016/S0168-583X(99)00637-0.

[35] R. Avakian, K. Avetyan, K. Ispirian, E. Melikian, Bent crystallographic planes in gradient crystals and crystalline undulators, Nucl. Instrum. Meth. Phys. Res. A 508 (3) (2003) 496–499, http://dx.doi.org/10.1016/S0168-9002(03)01656-5.

[36] W. Krause, A. Korol, A. Solov'yov, W. Greiner, Photon emission by ultra-relativistic positrons in crystalline undulators: the high-energy regime, Nucl. Instrum. Meth. Phys. Res. A 483 (1) (2002) 455–460, http://dx.doi.org/10.1016/S0168-9002(02)00361-3.

[37] H.J. Goldschmid, Interstitial Alloys, Butterworths, London, 1967, http://dx.doi.org/10.1007/978-1-4899-5880-8.

[38] M.N.R. Ashfold, P.W. May, C.A. Rego, N.M. Everitt, Thin film diamond by chemical vapour deposition methods, Chem. Soc. Rev. 23 (1994) 21–30, http://dx.doi.org/10.1039/CS9942300021.

[39] F. Brunet, P. Germi, M. Pernet, A. Deneuville, E. Gheeraert, F. Laugier, M. Burdin, G. Rolland, The effect of boron doping on the lattice parameter of homoepitaxial diamond films, Diam. Relat. Mater. 7 (6) (1998) 869–873, http://dx.doi.org/10.1016/S0925-9635(97)00316-6.

[40] K.W. Böer, U.W. Pohl, Crystal Defects, Springer International Publishing, Cham, 2020, pp. 1–54, http://dx.doi.org/10.1007/978-3-319-06540-3_15-4.

[41] A. Tallaire, V. Mille, O. Brinza, T.N. Tran Thi, J. Brom, Y. Loguinov, A. Katrusha, A. Koliadin, J. Achard, Thick CVD diamond films grown on high-quality type IIa HPHT diamond substrates from new diamond technology, Diam. Relat. Mater. 77 (2017) 146–152, http://dx.doi.org/10.1016/j.diamond.2017.07.002.

[42] B. Campbell, A. Mainwood, Radiation damage of diamond by electron and Gamma irradiation, Phys. Status Solidi (A) 181 (1) (2000) 99–107, http://dx.doi.org/10.1002/1521-396X(200009)181:1<99::AID-PSSA99>3.0.CO;2-5.

[43] B. Campbell, W. Choudhury, A. Mainwood, M. Newton, G. Davies, Lattice damage caused by the irradiation of diamond, Nucl. Instrum. Meth. Phys. Res. A 476 (3) (2002) 680–685, http://dx.doi.org/10.1016/S0168-9002(01)01664-3.

[44] M.D. Dickers, G.B. Sushko, A.V. Korol, N.J. Mason, F. Fantuzzi, A.V. Solov'yov, Dopant concentration effects on $Si_{1-x}Ge_x$ crystals for emerging light-source technologies: a molecular dynamics study, Eur. Phys. J. D. 78 (6) (2024) 77, http://dx.doi.org/10.1140/epjd/s10053-024-00870-2.

[45] I.A. Solov'yov, A.V. Yakubovich, P.V. Nikolaev, I. Volkovets, A.V. Solov'yov, MesoBioNano explorer–a universal program for multiscale computer simulations of complex molecular structure and dynamics, J. Comput. Chem. 33 (30) (2012) 2412–2439, http://dx.doi.org/10.1002/jcc.23086.

[46] G.B. Sushko, I.A. Solov'yov, A.V. Solov'yov, Modeling MesoBioNano systems with MBN studio made easy, J. Mol. Graph. Model. 88 (2019) 247–260, http://dx.doi.org/10.1016/j.jmgm.2019.02.003.

[47] V.L. Solozhenko, O.O. Kurakevych, D. Andrault, Y. Le Godec, M. Mezouar, Ultimate metastable solubility of boron in diamond: Synthesis of superhard diamondlike BC_5, Phys. Rev. Lett. 102 (2009) 015506, http://dx.doi.org/10.1103/PhysRevLett.102.015506.

[48] J. Tersoff, New empirical approach for the structure and energy of covalent systems, Phys. Rev. B 37 (1988) 6991–7000, http://dx.doi.org/10.1103/PhysRevB.37.6991.

[49] J. Tersoff, Modeling solid-state chemistry: Interatomic potentials for multicomponent systems, Phys. Rev. B 39 (1989) 5566–5568, http://dx.doi.org/10.1103/PhysRevB.39.5566.

[50] K. Matsunaga, C. Fisher, H. Matsubara, Tersoff potential parameters for simulating cubic boron carbonitrides, Japan. J. Appl. Phys. 39 (2000) http://dx.doi.org/10.1143/JJAP.39.L48.

[51] T. Saotome, K. Ohashi, T. Sato, H. Maeta, K. Haruna, F. Ono, Thermal expansion of a boron-doped diamond single crystal at low temperatures, J. Phys.: Condens. Matter. 10 (1998) 1267–1272.

[52] L. Vegard, Die konstitution der mischkristalle und die Raumfüllung der atome, Z. Für Phys. 5 (1) (1921) 17–26, http://dx.doi.org/10.1007/BF01349680.

[53] W. Hayami, T. Hiroto, K. Soga, T. Ogitsu, K. Kimura, Thermodynamic stability of elemental boron allotropes with varying numbers of interstitial atoms, J. Solid State Chem. 329 (2024) 124407, http://dx.doi.org/10.1016/j.jssc.2023.124407.

[54] V.V. Brazhkin, E.A. Ekimov, A.G. Lyapin, S.V. Popova, A.V. Rakhmanina, S.M. Stishov, V.M. Lebedev, Y. Katayama, K. Kato, Lattice parameters and thermal expansion of superconducting boron-doped diamonds, Phys. Rev. B 74 (2006) 140502, http://dx.doi.org/10.1103/PhysRevB.74.140502.

[55] E. Bustarret, E. Gheeraert, K. Watanabe, Optical and electronic properties of heavily boron-doped homo-epitaxial diamond, Phys. Status Solidi (A) 199 (1) (2003) 9–18, http://dx.doi.org/10.1002/pssa.200303819.

[56] T. Wojewoda, P. Achatz, L. Ortéga, F. Omnès, C. Marcenat, E. Bourgeois, X. Blase, F. Jomard, E. Bustarret, Doping-induced anisotropic lattice strain in homoepitaxial heavily boron-doped diamond, Diam. Relat. Mater. 17 (7) (2008) 1302–1306, http://dx.doi.org/10.1016/j.diamond.2008.01.040.

[57] A. Kawano, H. Ishiwata, S. Iriyama, R. Okada, T. Yamaguchi, Y. Takano, H. Kawarada, Superconductor-to-insulator transition in boron-doped diamond films grown using chemical vapor deposition, Phys. Rev. B 82 (2010) 085318, http://dx.doi.org/10.1103/PhysRevB.82.085318.

[58] K.T. Jacob, S. Raj, L. Rannesh, Vegard's law: a fundamental relation or an approximation? Int. J. Mater. Res. 98 (9) (2007) 776–779, http://dx.doi.org/10.3139/146.101545.

[59] E. Bourgeois, E. Bustarret, P. Achatz, F. Omnès, X. Blase, Impurity dimers in superconducting B-doped diamond: Experiment and first-principles calculations, Phys. Rev. B 74 (2006) 094509, http://dx.doi.org/10.1103/PhysRevB.74.094509.

[60] J.P. Goss, P.R. Briddon, R. Jones, Z. Teukam, D. Ballutaud, F. Jomard, J. Chevallier, M. Bernard, A. Deneuville, Deep hydrogen traps in heavily B-doped diamond, Phys. Rev. B 68 (2003) 235209, http://dx.doi.org/10.1103/PhysRevB.68.235209.

[61] J.P. Goss, P.R. Briddon, Theory of boron aggregates in diamond: First-principles calculations, Phys. Rev. B 73 (2006) 085204, http://dx.doi.org/10.1103/PhysRevB.73.085204.

[62] J.P. Goss, R.J. Eyre, P.R. Briddon, Bound substitutional impurity pairs in diamond: a density functional study, J. Phys.: Condens. Matter. 20 (8) (2008) 085217, http://dx.doi.org/10.1088/0953-8984/20/8/085217.

[63] T. Watanabe, S. Yoshioka, T. Yamamoto, H. Sepehri-Amin, T. Ohkubo, S. Matsumura, Y. Einaga, The local structure in heavily boron-doped diamond and the effect this has on its electrochemical properties, Carbon 137 (2018) 333–342, http://dx.doi.org/10.1016/j.carbon.2018.05.026.

[64] T. Lundström, B. Lönnberg, J. Bauer, Thermal expansion of β-rhombohedral boron, J. Alloys Compd. 267 (1) (1998) 54–58, http://dx.doi.org/10.1016/S0925-8388(97)00545-8.

[65] P. Jacobson, S. Stoupin, Thermal expansion coefficient of diamond in a wide temperature range, Diam. Relat. Mater. 97 (2019) 107469, http://dx.doi.org/10.1016/j.diamond.2019.107469.

[66] T. Halicioglu, (2×1) reconstructed patterns of diamond (100) surface, Diam. Relat. Mater. 1 (9) (1992) 963–967, http://dx.doi.org/10.1016/0925-9635(92)90118-8.

[67] G. Kern, J. Hafner, J. Furthmüller, G. Kresse, (2×1)Reconstruction and hydrogen-induced de-reconstruction of the diamond (100) and (111) surfaces, Surf. Sci. 352–354 (1996) 745–749, http://dx.doi.org/10.1016/0039-6028(95)01244-3.

[68] TECHNO-CLS Consortium, TECHNO-CLS Periodic Report: Reporting Period 3, Tech. rep., 2025, Horizon Europe EIC-Pathfinder Project TECHNO-CLS, internal report, Grant Agreement No. 101046458, unpublished.

[69] A. Netto, M. Frenklach, Kinetic Monte Carlo simulation of diamond film growth with the inclusion of surface migration, MRS Online Proc. Libr. 527 (1) (1998) 383–388, http://dx.doi.org/10.1557/PROC-527-383.

[70] W.J. Rodgers, P.W. May, N.L. Allan, J.N. Harvey, Three-dimensional kinetic Monte Carlo simulations of diamond chemical vapor deposition, J. Chem. Phys. 142 (21) (2015) 214707.

[71] A. Cheesman, J.N. Harvey, M.N.R. Ashfold, Computational studies of elementary steps relating to boron doping during diamond chemical vapour deposition, Phys. Chem. Chem. Phys. 7 (2005) 1121–1126, http://dx.doi.org/10.1039/B418664H.

[72] M. Lu, C. Zhang, F. Sun, Growth mechanisms and material properties of boron-doped single crystal diamond synthesized by HFCVD, Surf. Interfaces 62 (2025) 106217, http://dx.doi.org/10.1016/j.surfin.2025.106217.